

## **Memòria justificativa de recerca de les beques predoctorals per a la formació de personal investigador (FI)**

La memòria justificativa consta de les dues parts que venen a continuació:

- 1.- Dades bàsiques i resums
- 2.- Memòria del treball (informe científic)

Tots els camps són obligatoris

### **1.- Dades bàsiques i resums**

**Títol del projecte** ha de sintetitzar la temàtica científica del vostre document.

SIMULACIÓ NUMÈRICA DE FENÒMENS DE TRANSFERÈNCIA DE CALOR I DINÀMICA DE FLUIDS TRANSITORIS

#### **Dades de l'investigador (beneficiari de l'ajut)**

Nom DENIZ Cognoms KIZILDAG  
Correu electrònic deniz@cttc.upc.edu

#### **Dades del director del projecte**

Nom ASSENSI Cognoms OLIVA LLENA  
Correu electrònic oliva@cttc.upc.edu

#### **Dades de la universitat / centre al que s'està vinculat**

UNIVERSITAT POLITÈCNICA DE CATALUNYA / CENTRE TECNOLÒGIC DE TRANSFERÈNCIA DE CALOR (CTTC)

#### **Número d'expedient**

2006FI 01227

**Paraules clau:** cal que esmenteu cinc conceptes que defineixin el contingut de la vostra memòria.

natural convection, verification, non-boussinesq, LES, DNS

#### **Data de presentació de la justificació**

12.08.2010

**Resum en la llengua del projecte** (màxim 300 paraules)  
el resum i la memòria es presenten al fitxer "memoria.pdf"

**Resum en anglès**(màxim 300 paraules)

el resum i la memòria es presenten al fitxer "memoria.pdf"

---

**2.- Memòria del treball** (informe científic sense limitació de paraules). Pot incloure altres fitxers de qualsevol mena, no més grans de 10 MB cadascun d'ells.

el resum i la memòria es presenten al fitxer "memoria.pdf"

NUMERICAL SIMULATIONS OF  
TRANSIENT PHENOMENA IN HEAT  
TRANSFER AND FLUID DYNAMICS

Deniz Kizildag

July 2010

MEMÒRIA JUSTIFICATIVA DE RECERCA

## Resume

The work carried out during the 4 year research activity can be barely classified in two main lines. On the one hand, a considerable effort is taken to address issues related with the verification of multi-dimensional and transient solutions that are obtained by numerical simulations. Within the studied cases, we can consider cases of piston-cylinder flows within geometries similar to those of hermetic reciprocating compressors. This issue is mentioned in *Part I*. On the other hand, numerical simulations of different phenomena have been performed. More emphasis has been given to the natural convection flow within enclosures. This is explained in *Part II*.

The case extensively studied has been the natural convection flow. The natural convection flow within enclosures has attracted the attention of many researchers due to its potential to model numerous applications of engineering interest, such as cooling of electronic devices, air flow in buildings, heat transfer in solar collectors, among others. The natural convection studies corresponding to the parallelepipedic enclosures can be classified into two elementary classes: i) heating from a horizontal wall (heating from below); ii) heating from a vertical wall. The characteristic example of the former case is the Rayleigh-Bénard flow, however this research is on the cavities heated from the side. This configuration is referred commonly as the differentially heated cavity.

Although the differentially heated cavity configuration represents a simple geometry, the flow gets complex for sufficiently large Rayleigh numbers [1]. The flow undergoes a gradual transition to a chaotic state as the Rayleigh number reaches a critical value. For the situations studied in this research activity, both laminar, transitional, and turbulent zones are expected to coexist within the domain. Generally the core of the cavity together with the upstream part of the vertical boundary layers remain laminar while at some point in the downstream part of the vertical boundary layers, turbulent fluctuations become significant. It is a challenging task to detect this phenomenon [2]. Another important issue is the stratification phenomenon taking place in the core of the cavity. It is one of the basic open problems of this configuration. Comparisons between numerical and experimental studies give quite different results, which may be justified by the thermal radiation effects [3].

The vast majority of the performed work in this field corresponds to air-filled cavities (see [2] for a detailed preview). If the working fluid is water, obtaining solutions for the governing equations gets even more complicated, as the boundary layer becomes thinner than for air at the same conditions. As a consequence, there is an increasing demand for excessively fine grids in space and time for solving the three-dimensional and time dependent flow, in order to capture the smallest scales of the turbulent flow. Direct Numerical Simulations (DNS) can be limited to lower Rayleigh numbers and less time integration, however the use of Large-Eddy Simulations (LES) appears as an attractive alternative for the

resolution of natural convection problems at high Rayleigh numbers. It must be borne in mind that as LES performs a modelling for the smallest scales of the flow, the results are strongly dependent not only on grid resolution, but also on the selection of the appropriate subgrid scale stresses (SGS) model to describe the flow behaviour.

Additional to the issues explained above, when investigating the fluid behaviour in real working conditions, the validity of the Oberbeck-Boussinesq approximation has to be questioned. According to Gray and Giorgini [3], the use of the Oberbeck-Boussinesq approximation can be considered valid for variations of thermophysical properties up to 10% with respect to the mean value.

This work also addresses the verification of multi-dimensional and transient numerical solutions based on grid refinement studies and the Richardson extrapolation techniques. Different verification methods based on alternative extrapolation strategies, and on both the simultaneous and the independent refinement of coordinates are investigated. Extrapolation strategies studied encompass the generalized Richardson extrapolation (GRE) based on both the local and the global observed order of convergence, and the mixed-order Richardson extrapolation (MORE). Discussion has been carried out on the performance of each method for the verification of a manufactured solution (MMS), and both incompressible and compressible flows on different piston-cylinder configurations.

## Part I

# Verification of multi-dimensional and transient CFD solutions

Main contents of this part is published in:

Orozco C, Kizildag D, Oliva A, Perez-Segarra CD. Verification of Multidimensional and Transient CFD Solutions. Numerical Heat Transfer Part B-Fundamentals 2010;57:46-73. DOI: 10.1080/10407791003613702.

## Introduction

This work addresses the verification of multi-dimensional and transient numerical solutions based on Richardson extrapolation techniques. Alternative extrapolation strategies based on both simultaneous (SCR) and independent (ICR) space-and-time coordinates refinement studies are investigated. Extrapolation strategies studied encompass the generalized Richardson extrapolation (GRE) based on both the local and the global observed order of accuracy, and the mixed-order Richardson extrapolation (MORE). Performance of all verification methods investigated have been tested on a manufactured solution, and on the flows in different piston-cylinder configurations. Results reveal that the global observed order of accuracy, and the post-processing estimators obtained from ICR studies can provide useful information on which the most suitable verification methods can be selected.

## Verification procedure

The procedure here presented has been developed as an extension of the post-processing tool for the verification of steady-state solutions reported by Cadafalch et al. [4]. The tool is based on the GRE and the global observed value of  $p$ , and provides information on the both local and global estimations of the observed order of accuracy and the  $GCI$ . Initially all solutions are interpolated onto a common post-processing mesh. Nodes of this mesh are then classified into Richardson, oscillatory, and converged nodes depending on the local observed convergence behaviour. Local estimators of  $p$  are then calculated all the Richardson nodes, and of the  $GCI$  at both Richardson and converged nodes. This tool, based on SCR studies, can be applied to the verification of transient solutions by simply considering the time coordinate in the same way as the rest of the space coordinates. The present procedure includes additional grid extrapolation techniques, namely the GRE based on the local bounded  $p$ , the

GRE based on the global  $p$ , and the MORE. Furthermore, the procedure has also been further extended to ICR studies.

The procedure described below is divided in two parts. Part I applies to both SCR and ICR studies. For the latter, the procedure must be carried out for each independent coordinate direction. Information on the convergence associated with the discretization of each of these directions is provided. Part II exclusively applies to ICR studies, and provides the overall values of both the local and the global  $GCI$ .

### Part I (for SCR and ICR studies)

*Step 1. Interpolation at the post-processing mesh.* All three solutions are interpolated into the nodes of the grid where the estimators are calculated (the post-processing mesh), typically the coarsest grid. Special care is taken to avoid the introduction of additional uncertainties due to the interpolation process by using third-order accurate Lagrangian interpolation.

*Step 2. Classification of the calculation nodes.* All the calculation nodes of the post-processing mesh are classified into Richardson, converged or oscillatory nodes, according to the following definitions.

$$\begin{aligned} \text{Richardson node: } & \epsilon_{32}^*(\mathbf{x}, t) \cdot \epsilon_{21}^*(\mathbf{x}, t) > C_0 \\ \text{Converged node: } & |\epsilon_{32}^*(\mathbf{x}, t) \cdot \epsilon_{21}^*(\mathbf{x}, t)| \leq C_0 \\ \text{Oscillatory node: } & \epsilon_{32}^*(\mathbf{x}, t) \cdot \epsilon_{21}^*(\mathbf{x}, t) < -C_0 \end{aligned}$$

where the superscript  $*$  indicates that the solutions have been normalised by means of the maximum absolute value of  $\phi(\mathbf{x}, t)$ , and  $C_0$  is a positive coefficient approaching 0. As in the work by Cadafalch et al.  $C_0 = 10^{-30}$  is used in this work where computations have also been performed using double precision real numbers. It must be noted that the definition of Richardson nodes made in this classification coincides with that of nodes showing monotonic error convergence, rather than those where the asymptotic convergence requirement of the GRE is fulfilled.

*Step 3. Calculation of the local observed order of accuracy,  $p(\mathbf{x}, t)$ .* Local values of the observed order of accuracy  $p(\mathbf{x}, t)$  are calculated on Richardson nodes (see [5]).

*Step 4. Calculation of the global observed order of accuracy,  $p$ .* The global observed order of accuracy is evaluated by arithmetic averaging all values of the observed  $p(\mathbf{x}, t)$  at the Richardson nodes. The standard deviation of the local values from the mean values,  $\sigma_p$ , is also calculated.

*Step 5. Calculation of the local  $GCI$ .* The values of  $GCI(\mathbf{x}, t)$  are calculated for the solution obtained on the fine grid using a safety factor  $F_s = 1.25$ . Depending on the extrapolation technique adopted for the estimation of  $\phi_E(\mathbf{x}, t)$ , the following methods have been considered:

STD (standard) method. The local  $GCI$  is calculated at all the Richardson and converged nodes. At the Richardson nodes,  $GCI(\mathbf{x}, t)$  is evaluated using the extrapolated value (see [5]), assuming  $p(\mathbf{x}, t)$  to be equal to the global observed order of accuracy,  $p$ , calculated at Step 4. At the converged nodes  $GCI(\mathbf{x}, t)$  is assumed to be 0.

LP methods. Similar to the STD method, except for the estimation of  $p(\mathbf{x}, t)$ . This value is now calculated (see [5]) if contained within a certain range,  $p_L \leq p(\mathbf{x}, t) \leq p_U$ . Otherwise, the values of upper and lower bounds of this range,  $p_U$  and  $p_L$ , are used depending on whether  $p(\mathbf{x}, t)$  sits above or below of this range respectively. Depending on the values of  $p_L$  and  $p_U$ , three different variants are considered, LP12, LP13 and LP23, which are characterised by bounds  $1.0 \leq p(\mathbf{x}, t) \leq 2.0$ ,  $1.0 \leq p(\mathbf{x}, t) \leq 3.0$  and  $2.0 \leq p(\mathbf{x}, t) \leq 3.0$ , respectively.

MO methods. The local  $GCI$  is calculated from the mixed-order Richardson extrapolation (MORE) at all the post-processing mesh nodes. Two different methods have been considered. Method MO12 is based on the mixed first- and second-order extrapolation, and Method MO23 is based on the mixed second- and third-order extrapolation. See [5] for details.

*Step 6. Calculation of the global  $GCI$ .* The global value of the  $GCI$  is estimated by volume weighted averaging of the local values of the  $GCI$ . The global  $GCI$  is calculated from local values at the Richardson and the converged nodes for the STD and the LP methods. For MO methods, the global  $GCI$  is calculated from local values at all the post-processing mesh nodes. The standard deviation of the  $GCI$  can also be calculated.

## Part II (only for ICR studies)

*Step 1. Calculation of the local values of the overall  $GCI$ .* These values are calculated (see [5]) in all nodes of the post-processing mesh where the local  $GCI$  values could be estimated according to step 5 of Part I for all the independent coordinate directions.

*Step 2. Calculation of the global value of the overall  $GCI$ .* This value is calculated as:

$$GCI = GCI_x + GCI_y + GCI_z + GCI_t \quad (1)$$

where the terms on the r.h.s. of the equation correspond to the global  $GCI$  values (see step 6 of Part I) obtained in the respective coordinate directions (x, y, z, t).

It must be noted that, alternatively, the global value of the overall  $GCI$  (Part II, *Step 2*) could have also been calculated based on the volume averaging of the local values of the overall  $GCI$ . This option shows however a practical disadvantage. If GRE is used for extrapolation in different coordinate directions, the number of nodes where the local  $GCI$  can be calculated for each one

of the independent coordinates can be, in practice, quite reduced. As a result, in general, less reliable global values of the overall  $GCI$  can be obtained.

## Tested cases

The following test cases have been selected to assess the accuracy and the conservativeness of the verification methods discussed in this work. The first case is based on the method of manufactured solutions (MMS)[6]. This method forces the governing equations to provide a certain manufactured analytical solution, regardless of its physical realism, by including the required additional source terms. The accuracy and the conservativeness of the estimators obtained from the different verification methods being studied can therefore be assessed by simply comparison with the values of the exact error. In the second and third cases the fluid flow on two different piston-cylinder configurations are studied.

The solutions of all three test cases have been computed using the Finite Volume method based on staggered arrangement of variables. The segregated SIMPLEC [7] algorithm has been used to deal with the pressure-velocity coupling. The calculation domains have been discretized using Cartesian moving grids. The hybrid SMART scheme is used in the discretization of the convective term, while CDS is used for the diffusive term, and formally second-order methods for the remaining terms. Both first- (1OT) and second-order (2OT), fully implicit discretizations have been used for time discretization. Satisfaction of the discrete space conservation law has been enforced. The sets of grids used in the discretization of each case are tabulated in Table 3. A well verified code, namely DPC [4], has been used to perform the computation of the solutions of all three test cases. Let test case A serve just as an example of the thorough verification testing that have been conducted on this code.

Cases A and C				Case B			
space grid		time grid		space grid		time grid	
level	size	level	size	level	size	level	size
m1	6x6	t1	60	m1	10x20	t1	204
m2	12x12	t2	120	m2	19x41	t2	408
m3	24x24	t3	240	m3	38x82	t3	816
m4	48x48	t4	480	m4	76x164	t4	1632
m5	96x96	t5	960	m5	152x328	t5	3264
m6	192x192	t6	1920	m6	304x656	t6	6528

Table 1: Space and time discretization grids used in the test cases.

## Case A: Manufactured solution

The MMS is applied to the axisymmetric, incompressible continuity and momentum equations. The proposed manufactured solution is:

$$v_r = V_0 \sin(r)\sin(z)\sin(t) \quad (2)$$

$$v_z = V_0 \frac{\cos(z)\sin(t)(\sin(r) + r\cos(r))}{r} \quad (3)$$

$$p = r^3 + z^3 \quad (4)$$

where  $r$  and  $z$  are the radial and axial components of the position vector respectively,  $t$  is the time,  $v_r$  and  $v_z$  are the radial and axial components of the velocity vector,  $p$  is pressure, and  $V_0$  is a reference velocity equal to 1. The equations are solved in the domain  $D = \{(r, z) \mid r \in [\pi, 2\pi], z \in [0, 2\pi]\}$  from the initial instant  $t_0 = 0$  to the final instant  $t_f = 6$ . The calculation domain is discretized using moving grids with fixed boundaries. The motion of the mesh is achieved by varying the concentration of the nodes towards the boundaries on each direction. The grid concentration is controlled by the hyperbolic tangent concentration function reported by Prez-Segarra et al. [8] using a grid concentration factor  $\gamma = \sin(t)$ . Uniform grid has been used for time discretization. A Reynolds number ( $Re = \rho V_0 \pi / \mu$ ) of  $100\pi$  has been used. Dirichlet boundary conditions are determined from the manufactured solution. As an illustrative example of the manufactured solution studied, a plot of the stream-traces at the instant  $t/t_f=0.75$  is given in Figure 1.

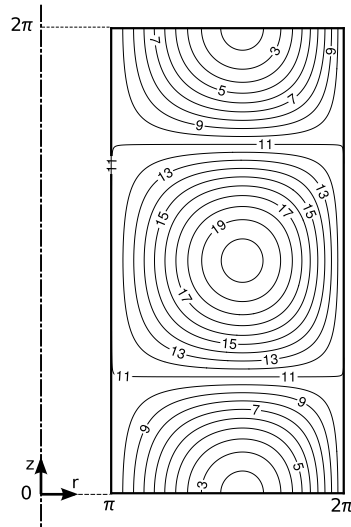


Figure 1: Case A. Manufactured solution. Stream-traces at time instant  $t/t_f=0.75$

## Case B: Incompressible flow on a piston-cylinder assembly

The incompressible, laminar, axisymmetric flow on the piston-cylinder assembly proposed by Durst et al. [9, 10] is analysed. Figure 2 shows the geometry of the configuration under study. Flow starts from rest at  $t=0$ , and the piston suddenly accelerates to its final velocity  $V_p$ . The characteristic dimensions of the domain sketched in Figure 2 are  $l_i=100\text{mm}$ ,  $d_i=19\text{mm}$  and  $d_p=45\text{mm}$ . The initial piston clearance is 40mm at  $t=0$ , and moves at  $V_p=11.9\text{mm/s}$  during 2.04 seconds. The Reynolds number, defined as  $Re = \rho V_P d_i / \mu$ , is 98. In the inlet boundary condition, the axial velocity has been assumed to be uniform, and the radial velocity to be zero. Non-slip boundary condition has been considered in the walls of the channel, the cylinder and the piston head. The domain has been divided in the three different blocks shown in Figure 2 and a uniform grid has been used for the discretization of each block. Uniform time-steps have been employed in time coordinate discretization.

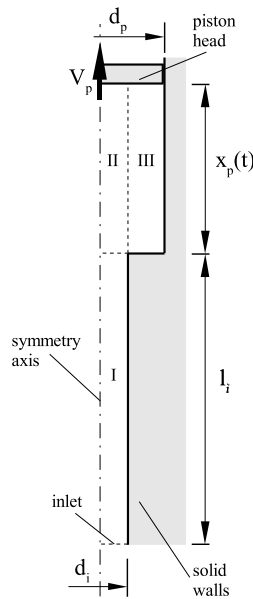


Figure 2: Case B. Incompressible flow on a piston-cylinder assembly.

## Case C: Gas spring

The two-dimensional, compressible flow in a closed piston-cylinder configuration is studied. Figure 3 sketches the geometry of the calculation domain, where the piston diameter and stroke are  $d_p=50.80\text{mm}$  and  $L=76.2\text{mm}$  respectively. The piston moves at 10r.p.m. following a sinusoidal law, with a compression ratio



Description	Acronyms
Simultaneous space-and-time coordinates refinement studies (SCR)	
GRE based on the global $p$ ( <i>standard method</i> )	STD
GRE based on the local $p$ ( <i>LP methods</i> )	
$1 \leq p \leq 2$	PL12
$1 \leq p \leq 3$	PL13
$2 \leq p \leq 3$	PL23
Mixed-order Richardson extrapolation ( <i>MORE method</i> )	
First- and second-order	MO12
Second- and third-order	MO23
Independent coordinate refinement studies (ICR)	
HREF and TREF studies based on STD method	ICR-STD

Table 2: Acronyms corresponding to the different verification methods. Note: HREF and TREF refer to grid refinement in space and time coordinates respectively

expected limits were obtained.

It has also been highlighted that the formal order of accuracy of the discretization method is not sufficient information to select the most adequate limits of  $p$  to be used in the LP methods, or the error terms to be considered in the MO methods. Additional information on how the solution is converging is therefore also required. Such information can in some cases be provided by the global observed  $p$ . However, the limitations of this estimator in cases of mixed-order convergence must be borne in mind. These limitations can be partially overcome by the information obtained from ICR studies in cases of mixed-order convergence originated by the different-order discretization of the space and time coordinates. An alternative expression to that proposed by Roache for the estimation of the overall value of the  $GCI$  in ICR studies has also been briefly discussed and assessed. Despite the satisfactory results presented, a deeper investigation on its performance for verification purposes and on the adequate value of  $F_s$  is required.

Finally, different cases have been identified where the estimated value of the global  $p$  systematically suggests second-order convergence in consecutive grid levels, which might be interpreted as convergence approaching the second-order asymptotic limit. However, discrepancies obtained in some cases amongst solutions provided from different methods, e.g. MO12 and MO23, suggest that solution might be actually converging far from second-order asymptotic range. The correct use of  $p$  as a representative indicator of the real solution convergence on which the most adequate verification techniques can be selected, and its dependency on the observed value of  $\sigma_p$ , needs therefore to be further investigated.



## Part II

# Non-Oberbeck-Boussinesq natural convection in a tall differentially heated cavity

Main contents of this part is published in:

Kizildag, D. and Ventosa, J. and Rodriguez, I. and Oliva, A. Non-Oberbeck-Boussinesq natural convection in a tall differentially heated cavity, *Fifth European Conference on Computational Fluid Dynamics ECCOMAS CFD 2010* June 14th - 17th, 2010 Lisbon, Portugal.

## Introduction

The natural convection flow within enclosures has attracted the attention of many researchers due to its potential to model numerous applications of engineering interest, such as cooling of electronic devices, air flow in buildings, heat transfer in solar collectors, among others. The natural convection studies corresponding to the parallelepipedic enclosures can be classified into two elementary classes: i) heating from a horizontal wall (heating from below); ii) heating from a vertical wall. The characteristic example of the former case is the Rayleigh-Bnard flow, however this research is on the cavities heated from the side. This configuration is referred commonly as the differentially heated cavity.

Although the differentially heated cavity configuration represents a simple geometry, the flow gets complex for sufficiently large Rayleigh numbers [1]. The flow undergoes a gradual transition to a chaotic state as the Rayleigh number reaches a critical value. For the situations studied in this research activity, both laminar, transitional, and turbulent zones are expected to coexist within the domain. Generally the core of the cavity together with the upstream part of the vertical boundary layers remain laminar while at some point in the downstream part of the vertical boundary layers, turbulent fluctuations become significant. It is a challenging task to detect this phenomenon [2]. Another important issue is the stratification phenomenon taking place in the core of the cavity. It is one of the basic open problems of this configuration. Comparisons between numerical and experimental studies give quite different results, which may be justified by the thermal radiation effects [2].

The vast majority of the performed work in this field corresponds to air-filled cavities (see [2] for a detailed preview). If the working fluid is water, obtaining solutions for the governing equations gets even more complicated, as the boundary layer becomes thinner than for air at the same conditions. As a consequence,

there is an increasing demand for excessively fine grids in space and time for solving the three-dimensional and time dependent flow, in order to capture the smallest scales of the turbulent flow. Direct Numerical Simulations (DNS) can be limited to lower Rayleigh numbers and less time integration, however the use of Large-Eddy Simulations (LES) appears as an attractive alternative for the resolution of natural convection problems at high Rayleigh numbers. It must be borne in mind that as LES performs a modelling for the smallest scales of the flow, the results are strongly dependent not only on grid resolution, but also on the selection of the appropriate subgrid scale stresses (SGS) model to describe the flow behaviour.

Additional to the issues explained above, when investigating the fluid behaviour in real working conditions, the validity of the Oberbeck-Boussinesq approximation has to be questioned. According to Gray and Giorgini [3], the use of the Oberbeck-Boussinesq approximation can be considered valid for variations of thermophysical properties up to 10% with respect to the mean value.

## Mathematical formulation and numerical method

The Navier-Stokes and continuity equations can be written as

$$\mathbf{M}\mathbf{u} = \mathbf{0} \quad (5)$$

$$\frac{\partial \mathbf{u}}{\partial t} + \mathbf{C}(\mathbf{u})\mathbf{u} + \nu \mathbf{D}\mathbf{u} + \rho^{-1}\mathbf{G}\mathbf{p} + \mathbf{f} = \mathbf{0} \quad (6)$$

$$\frac{\partial \mathbf{T}}{\partial t} + \mathbf{C}(\mathbf{u})\mathbf{T} + \rho^{-1}Cp^{-1}k\mathbf{D}(\mathbf{T}) = \mathbf{0} \quad (7)$$

where  $\mathbf{u} \in \mathbb{R}^{3m}$  and  $\mathbf{p} \in \mathbb{R}^m$  are the velocity vector and pressure, respectively (here  $m$  applies for the total number of control volumes (CV) of the discretised domain),  $\nu$  is the kinematic viscosity and  $\rho$  the density.  $\mathbf{f}$  is the body force  $\mathbf{f} = \beta(T_0 - T_m)\mathbf{g}$ . Convective and diffusive operators in the momentum equation for the velocity field are given by  $\mathbf{C}(\mathbf{u}) = (\mathbf{u} \cdot \nabla) \in \mathbb{R}^{3m \times 3m}$ ,  $\mathbf{D} = \nabla^2 \in \mathbb{R}^{3m \times 3m}$  respectively. Gradient and divergence (of a vector) operators are given by  $\mathbf{G} = \nabla \in \mathbb{R}^{3m \times 3m}$  and  $\mathbf{M} = \nabla \cdot \in \mathbb{R}^{m \times 3m}$  respectively.

In bouyancy driven flows a common approach is to consider constant thermo-physical properties of the fluid, with the exception of the density variations that are only taken into account in the bouyancy forces, i.e., the so-called Oberbeck-Boussinesq approximation. Thus, the temperature dependency of density is linearized in the bouyancy force as:

$$\rho(T) = \rho_m - \rho_m\beta_m(\mathbf{T} - T_m) \quad (8)$$

Here  $T_m = (T_h - T_c)/2$  is the mean value of the temperatures of the cold and hot walls. Those assumptions have its own implications. First, continuity

equation is treated in its incompressible form, neglecting acoustic phenomena, which in the case of liquids has no major implications. However, for liquids, deviations from the aforementioned hypothesis are mainly due to viscosity variations, as the viscosity strongly decreases with the temperature increase.

When considering these effects (Non-Oberbeck-Boussinesq effects) in our work, the following are assumed:

- temperature dependent thermophysical properties
- density variations are only taken into account in the bouyancy term
- the temperature dependence of the density is linearized as:

$$\rho(T) = \rho_m - \rho'(T) \quad (9)$$

Under the above assumptions, equations 1-3 read:

$$\mathbf{M}\mathbf{u} = \mathbf{0} \quad (10)$$

$$\frac{\partial \mathbf{u}}{\partial t} + \mathbf{C}(\mathbf{u})\mathbf{u} + \mathbf{D}(\nu(T)\mathbf{u}) + \rho_m^{-1}\widehat{\mathbf{G}}\mathbf{p} - \rho_m^{-1}\rho'(T)\mathbf{g} = \mathbf{0} \quad (11)$$

$$\frac{\partial \mathbf{T}}{\partial t} + \mathbf{C}(\mathbf{u})\mathbf{T} + \rho_m^{-1}Cp_m^{-1}\mathbf{D}(k(T)\mathbf{T}) = \mathbf{0} \quad (12)$$

The temperature dependencies for  $\nu(T)$ ,  $k(T)$  and  $\rho(T)$  are taken from Furukawa.[11]

Considering the reference scales for length, time, velocity, temperature and dynamic pressure as  $H$ ,  $(H^2/\alpha)Ra^{-0.5}$ ,  $(\alpha/H)Ra^{0.5}$ ,  $T_h - T_c$ ,  $\rho(\alpha/H^2)Ra$ , respectively, Non-Oberbeck-Boussinesq thermal convection in the cavity is governed by the non-dimensional quantities:  $Ra = (g\beta_m\Delta T_{ref}H^3Pr_m)/\nu_m^2$ ,  $Pr_m = \nu_m/\alpha_m$ ,  $\Gamma$  and the non-dimensional thermophysical properties:  $\nu^* = \nu(T)/\nu_m$ ;  $k^* = k(T)/k_m$ ;  $\rho^* = \frac{\rho_m - \rho(T)}{\rho_m\beta_m\Delta T_{ref}} = \frac{\rho'(T)}{\rho_m\beta_m\Delta T_{ref}}$ .

The governing equations are discretized on a collocated unstructured grid arrangement, by means of second-order spectro-consistent schemes [12]. Such discretization preserves the symmetry properties of the continuous differential operators, i.e., the conservation properties are held if, the convective term is discretized by a skew-symmetric operator and the diffusive term is approximated by a symmetric, positive-definite coefficient matrix. These properties ensure both, stability and conservation of the global kinetic-energy balance on any grid. Energy transport is also discretized by means of a spectro-consistent scheme. An explicit third-order Gear-like scheme [13] based on a fractional step method is used for time-advancement algorithm, except for the pressure gradient where a first-order backward Euler scheme is used.

Collocated meshes do not conserve kinetic energy when fractional step method is used [14, 15]. The source of these errors are interpolation schemes and inconsistency in the pressure field, in order to ensure mass conservation. While the first is eliminated through the use of conservative schemes, the latter equals to  $\epsilon_{ke} = (\tilde{\mathbf{p}}_c)^* \mathbf{M}_c (\mathbf{G}_c - \mathbf{G}_s) \tilde{\mathbf{p}}_c$ . Felten and Lund [15] showed that pressure errors are of the order of  $\mathcal{O}(\Delta x^2 \Delta t)$ . However, these errors do not have significant impact on the grid resolutions and time-steps used in LES and DNS.

LES studies have been performed using two different SGS models: i) the dynamic eddy viscosity model (DEV)[16] ii) the wall-adapting local-eddy viscosity (WALE)[17]. In order to study the influence of the models, a course DNS (CDNS) is also calculated.

## Problem definition

### Geometry

The adopted geometry considered in this work is shown in Figure 1. This geometry models the parallelepiped tank of an integrated solar collector. The height of the tank (H), and the width (W) are 0.735m and 0.11m respectively, resulting in an aspect ratio of  $\Gamma = 6.68$ .

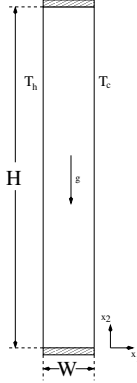


Figure 4: Geometry of the differentially heated cavity

Taking into consideration the real working conditions of the studied prototype, the temperatures at the hot and cold vertical isothermal walls are set to  $57^\circ\text{C}$  and  $47^\circ\text{C}$  respectively.

### Boundary conditions

For the velocities, no-slip condition is applied on all the walls. In the spanwise direction (when applicable) periodic boundary condition is used.

Isothermal vertical walls are assumed. Left vertical wall is at  $57\text{ }^\circ\text{C}$  and right vertical wall is at  $47\text{ }^\circ\text{C}$ . In the top and bottom confining walls, Neumann boundary condition ( $\partial T/\partial n = 0$ ) is applied.

Except for the Non-Oberbeck-Boussinesq calculations, the fluid properties for water are calculated at the average temperature of  $(T_h - T_c)/2 = 52\text{ }^\circ\text{C}$ . Rayleigh number based on the height of the cavity is  $Ra = \rho\beta(T_h - T_c)H^3/\nu\alpha = 2.2 \times 10^{11}$  and the Prandtl number is  $Pr = \nu/\alpha = 3.42$ , being  $\nu$  is the kinematic viscosity and  $\alpha$  thermal diffusivity.

## Fluid properties

For the Non-Oberbeck-Boussinesq calculations, the expressions in Furukawa [11] are used.

## Geometric discretization

The smallest scales at the hot and cold walls are imposed by viscous and thermal boundary layers, while grid size at the bulk must be lesser than Kolmogorov scale. For the Prandtl number in our problem, the thermal boundary layer is thinner than the viscous boundary layer as  $\delta_t \sim h/Ra^{0.25}$  and  $\delta_v \sim Pr^{0.5}\delta_t$  [18]. The meshes shown in Table 3 are used for our preliminary studies.

level	$N_1$	$\Delta x_{1min}$	$N_2$	$\Delta x_{2min}$	$\Delta t$
m1	80	$4.08 \times 10^{-5}$	250	$4 \times 10^{-3}$	$9.12 \times 10^{-6}$
m2	176	$8.16 \times 10^{-5}$	550	$1.82 \times 10^{-3}$	$3.65 \times 10^{-5}$
m3	258	$6.80 \times 10^{-5}$	770	$1.30 \times 10^{-3}$	$2.53 \times 10^{-5}$
m4	534	$4.08 \times 10^{-5}$	1870	$5.35 \times 10^{-4}$	$9.15 \times 10^{-6}$

Table 3: Space and time discretization grids used in the test cases.

## Preliminary results and conclusions

As the numerical effort to carry out the present simulations is too large, all the calculations here presented are restricted to two-dimensional (2D) simulations. Although 2D calculations might affect the fluid dynamics, some of the characteristics of the flow or non-Oberbeck-Boussinesq effects can still be captured under this assumption. It has been shown earlier by Trias et al. [2] for a differentially heated cavity for Rayleigh numbers up to  $10^{10}$  and by Schmalz et al. [19] for Rayleigh-Benard convection, that in general as a rough approach to capture the general features of the flow and especially boundary layer profiles and Nusselt

numbers, 2D simulations can be a good approximation. This is particularly true for comparisons of the non-Oberbeck-Boussinesq effects, where no SGS model has been used. However, regarding to LES modelling, some of the conclusions drawn in the present work must be taken as preliminary results, as the filtering process might be affected by the 2D assumptions done.

In order to study the Non-Oberbeck-Boussinesq effects,  $m_2$  grid size is used. The presented results correspond to a time integration of 100 time units starting from  $t_{ini} = 250$ .

First results show clearly that the employment of Oberbeck-Boussinesq approximation affects the thermal and fluid dynamic behaviour of the numerical solution. The influence of considering variable thermophysical properties can be appreciated in Figure 5. On the left, temperature profiles over  $x_2 = 0.5$  is plotted. Temperature at the core of the cavity is significantly greater in Non-Oberbeck-Boussinesq solution ( $T_{cNOB} > T_{cOB}$ ). On the right, vertical velocity profile is shown. It can be observed that there is no symmetry in Non-Oberbeck-Boussinesq solution. Boundary layer thickness differs in hot and cold vertical walls. In Figures 6 and 7 isotherms at representative instants for both cases are presented. In these figures, the aforementioned differences can be observed.

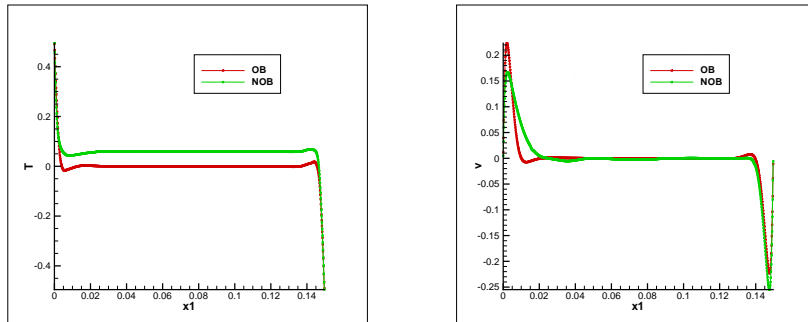


Figure 5: Temperature (left) and vertical velocity (right) profiles at  $x_2 = 0.5$

Although some three dimensional simulations have been carried out, the results are not shown here. The present work is intended to be a starting point for our study of non-Oberbeck-Boussinesq effects in turbulent natural convection.

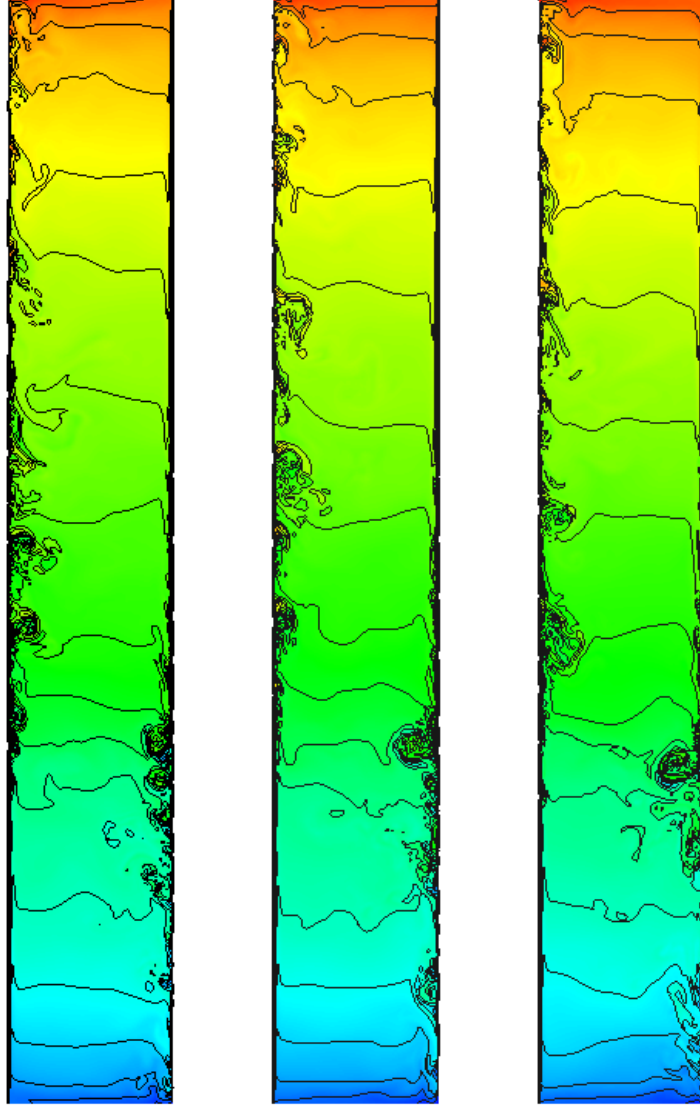


Figure 6: Representative instantaneous isotherms for non-Oberbeck-Boussinesq solution using  $m_2$  mesh. (left)  $t = 300$ , (middle)  $t = 350$ , (right)  $t = 400$ . The isotherms are uniformly distributed from -0.5 to 0.5

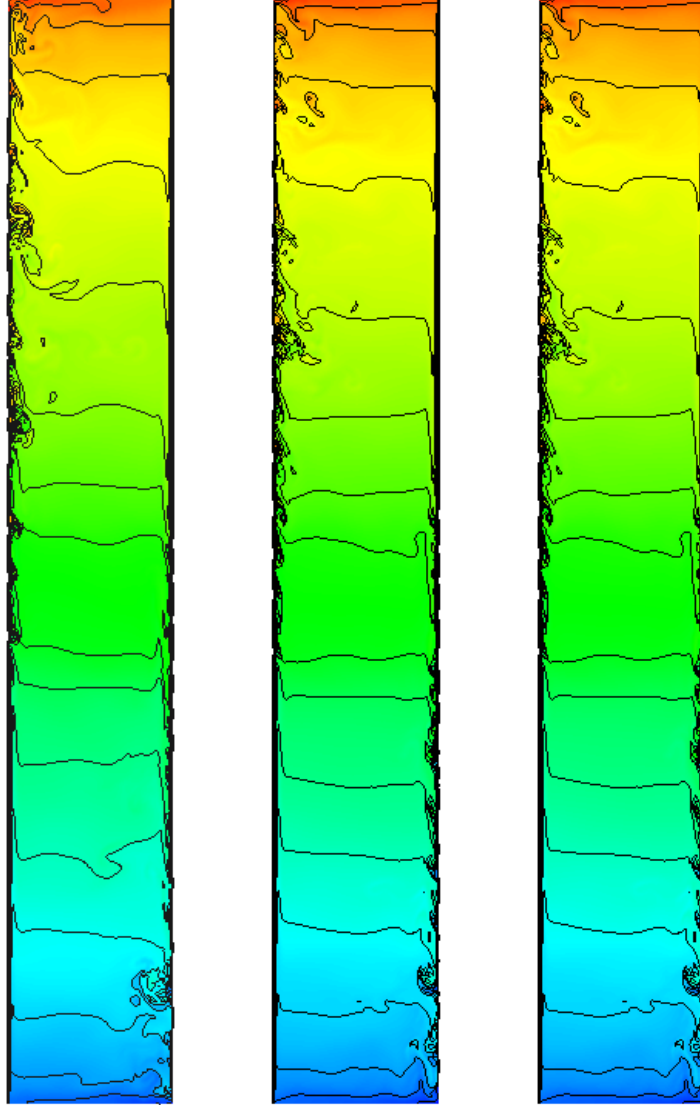


Figure 7: Representative instantaneous isotherms for Oberbeck-Boussinesq solution using  $m_2$  mesh. (left)  $t = 300$ , (middle)  $t = 350$ , (right)  $t = 400$ . The isotherms are uniformly distributed from -0.5 to 0.5

## References

- [1] D.G. Barhaghi and L. Davidson. Natural convection boundary layer in a 5:1 cavity. *Physics of Fluids*, 19(125106), 2007.
- [2] X. Trias, M. Soria, D. Perez-Segarra, and A. Oliva. Direct Numerical simulations of two and three dimensional turbulent natural convection flows in a differentially heated cavity of aspect ratio 4. *Journal of Fluid Mechanics*, 586:259–293, 2007.
- [3] D.D. Gray and A. Giorgini. The Validity of Boussinesq Approximation for Liquids and Gases. *Int. J. Heat Mass Transfer*, 19:545–551, 1976.
- [4] J. Cadafalch, C.D. Pérez-Segarra, R. Cònsul, and A. Oliva. Verification of finite volume computations on steady state fluid flow and heat transfer. *Journal of Fluids Engineering*, 124:11–21, 2002.
- [5] C. Orozco, D. Kizildag, A. Oliva, and C.D. Perez-Segarra. Verification of multidimensional and transient cfd solutions. *Numerical Heat Transfer Part BFundamentals*, 57:46–73, 2010.
- [6] P.J. Roache. Code verification by the method of manufactured solutions. *Journal of Fluids Engineering*, 124:4–10, 2002.
- [7] J.P. Van Doormal and G.D. Raithby. Enhancements of the simple method for predicting incompressible fluid flows. *Numerical Heat Transfer*, 7:147–163, 1984.
- [8] C.D. Pérez-Segarra, A. Oliva, M. Costa, and F. Escanes. Numerical experiments in turbulent natural and mixed convection in internal flows. *International Journal for Numerical Methods for Heat and Fluid Flow*, 5(1):13–33, 1995.
- [9] F. Durst, T. Maxworthy, and J.C.F. Pereira. Piston-driven, unsteady separation at a sudden expansion in a tube: Flow visualization and lda measurements. *Physics of Fluids*, 1(7):1249–1260, 1989.
- [10] H. Strll, F. Durst, M. Peric, J.C.F Pereira, and G. Scheuerer. Study of Laminar, Unsteady Piston-Cylinder Flow. *Journal of Fluids Engineering*, 115(4):687–693, 1993.
- [11] M. Furukawa. Practical expressions for thermodynamic and transport properties of commonly used fluids. *Journal of Thermophysics*, 5(4):524–531, 1991.
- [12] R. W. C. P. Verstappen and A. E. P. Veldman. Symmetry-Preserving Discretization of Turbulent Flow. *Journal of Computational Physics*, 187:343–368, May 2003.

- [13] G.M. Fishpool and M.A. Leschziner. Stability bounds for explicit fractional-step schemes for the Navier-Stokes equations at high Reynolds number. *Computers and Fluids*, 38:1289–1298, 2009.
- [14] Y. Morinishi, T.S. Lund, O.V. Vasilyev, and P. Moin. Fully conservative higher order finite difference schemes for incompressible flow. *Journal of Computational Physics*, 143(1):90–124, 1998.
- [15] F.N. Felten and T.S. Lund. Kinetic energy conservation issues associated with the collocated mesh scheme for incompressible flow. *Journal of Computational Physics*, 215(2):465–484, 2006.
- [16] M. Germano, U. Piomelli, P. Moin, and W.H. Cabot. A dynamic subgrid-scale eddy viscosity model. *Physics of Fluids A*, 3(1760), 1991.
- [17] F. Nicoud and F. Fucros. Subgrid-scale stress modelling based on the square of the velocity gradient tensor. *Flow, Turbulence and Combustion*, 62:183–200, 1999.
- [18] J. Patterson and J. Imberger. Unsteady natural convection in a rectangular cavity. *J. Fluids Mech.*, 100:65–86, 1980.
- [19] J. Schmalzl, M. Breuer, and U. Hansen. On the validity of two-dimensional numerical approaches to time-dependent thermal convection. *Europhys. Lett.*, 67 (3):390–396, 2004.